Rev. Chilena Hist. Nat. **71**, 593 (1998); M. T. K. Arroyo *et al.*, *Gayana Bot.* **55**, 93 (1999).

5. Ages are reported as calendar kiloyears B.P. All ^{14}C dates in the text and figures were converted to calendar ages with the program CALIB: v 4.0 (Intcal98) [M. Stuiver and P. J. Reimer, *Radiocarbon* **35**, 215 (1993)]. Grass abundance was measured as point occurrence on a 120-cell rectangular grid overlain on a sorting tray. A sediment matrix splitter was used to randomly segregate 100 ml of plant debris from each midden. Midden debris was spread uniformly across a 120-cell rectangular grid (each cell is 1 inch by 1 inch or ~6.45 cm^2); grass abundance was measured as point occurrence on the grid (the number of cells out of 120 where grass blades, florets, or seeds were identified). All plant remains were identified to the highest taxonomic level possible with a reference collection gleaned from herbarium specimens and our own field studies. In general, we met comparable success as with identifications of plant macrofossils in North American packrat middens.
6. Vascular plant remains, visible as carbonized wood, twigs, and leaves, are abundant in the wetland deposits. Other organic-rich samples are too fine grained or decomposed to identify the source and could suffer from hard-water effects on ^{14}C dates if partly algal in origin. Groundwater from springs in the Atacama displays hard-water or reservoir effects, typically containing $\leq 26\,^{14}C$ % modern carbon [R. Aravena and D. Suzuki, *Water Resources Res.* **26**, 2887 (1990)]. Evidence against a hard-water effect includes excellent stratigraphic coherence between dates from carbonized wood and other fine-grained organic matter and a date of 105 ^{14}C years B.P. on humates from a modern black mat.
7. M. Grosjean, *Palaeogeogr. Palaeoclimatol. Palaeoecol.* **109**, 89 (1994); M. Grosjean, M. A. Geyh, B. Messerli, U. Schotterer, *J. Paleolimnol.* **14**, 241 (1995).
8. M. Geyh *et al.*, *Quat. Res.* **52**, 143 (1999).
9. Extensive paleowetland deposits dating to the mid-Holocene are present on both the Rio Salado and Rio Loa, located 150 km north-northwest of Tilomonte. Mid-Holocene wetland deposits crop out 5 to 7 m above the modern wetlands. At the Rio Loa, the base of these deposits is not exposed, whereas samples from the middle and top of the section yielded ages of 4.9 and 3.5 ky B.P. Upper portions of the mid-Holocene wetland deposits at Rio Salado yielded ages between 6.7 and 4.3 ky B.P. Wetland deposits at Quebrada Puripica, dating between 7.1 and 4.4 ky B.P., were initially interpreted as paleowetland deposits formed from side-canyon damming by debris flows [M. Grosjean, L. Nuñez, I. Cartajena, B. Messerli, *Quat. Res.* **48**, 239 (1997)]. We found that the wetland deposits at Puripica were not debris-flow dammed but instead are similar to the deposits at Tilomonte and formed as a result of higher groundwater levels during the mid-Holocene.
10. M. Servant and J. C. Fontes, *Cah. ORSTOM Ser. Geol.* **10**, 5 (1978); B. Rondeau, thesis, Université du Québec à Montréal (1990); C. Clapperton, *Palaeogeogr. Palaeoclimatol. Palaeoecol.* **101**, 189 (1993); B. G. Bills *et al.*, *Geophys. Res. Lett.* **21**, 293 (1994); T. A. Blodgett, J. D. Lenters, B. L. Isacks, *Earth Interactions* **1** (1997) (http://ams.allenpress.com/amsonline/?request-get-archive&issn-1087-3562).
11. F. Sylvestre *et al.*, *Quat. Res.* **51**, 54 (1999).
12. D. T. Rodbell and G. O. Seltzer, *Quat. Res.*, in press.
13. D. Wirrmann and L. Oliveira, *Palaeogeogr. Palaeoclimatol. Palaeoecol.* **59**, 315 (1987); D. Wirrmann and P. Mourguiart, *Quat. Res.* **43**, 344 (1997); M. B. Abbott, M. W. Binford, M. Brenner, K. R. Kelts, *Quat. Res.* **47**, 169 (1997); P. Mourguiart *et al.*, *Palaeogeogr. Palaeoclimatol. Palaeoecol.* **143**, 51 (1998); G. O. Seltzer, P. Baker, S. Cross, R. Dunbar, S. Fritz, *Geology* **26**, 167 (1998); S. L. Cross, P. A. Baker, G. O. Seltzer, S. Fritz, R. B. Dunbar, *Holocene* **10**, 21 (2000).
14. L. G. Thompson *et al.*, *Science* **282**, 1858 (1998).
15. B. L. Valero-Garces *et al.*, *J. Paleolimnol.* **16**, 1 (1996); A. Schwalb, S. J. Burns, K. Kelts, *Palaeogeogr. Palaeoclimatol. Palaeoecol.* **148**, 153 (1999).
16. P. C. Baucom and C. A. Rigsby, *J. Sediment. Res.* **69**, 597 (1999).
17. C. A. Baied and J. C. Wheeler, *Mountain Res. Dev.* **13**, 145 (1993).
18. J. Chappellaz *et al.*, *Nature* **345**, 127 (1990); J. Chappellaz *et al.*, *Nature* **366**, 443 (1993); T. Blunier *et al.*, *Nature* **374**, 46 (1995).
19. A. Berger and M. F. Loutre, *Quat. Sci. Rev.* **10**, 297 (1991).
20. L. Martin *et al.*, *Quat. Res.* **47**, 117 (1997); M. B. Abbott, G. O. Seltzer, K. Kelts, J. Southon, *Quat. Res.* **47**, 70 (1997); G. Seltzer, D. Rodbell, S. Burns, *Geology* **28**, 35 (2000).
21. J. D. Lenters and K. H. Cook, *Mon. Weather Rev.* **127**, 409 (1999); R. D. Garreaud, *Mon. Weather Rev.* **127**, 901 (1999); M. Vuille, *Int. J. Climatol.* **19**, 1579 (1999); M. Vuille, R. S. Bradley, F. Keiming, *J. Geophys. Res.* **105**, 12447 (2000).
22. Z. Liu *et al.*, *PAGES Newsl.* **2**, 16 (1999).
23. A. C. Clement, R. Seager, M. Cane, *Paleoceanography* **14**, 441 (1999); M. Cane and A. C. Clement, in *Mechanisms of Global Climate Change at Millennial Time Scales*, vol. 112 of *Geophysical Monograph Series*, P. U. Clark, R. S. Webb, L. D. Keigwin, Eds., (American Geophysical Union, Washington, DC, 1999), pp. 373–383.
24. E. J. Brook, T. Sowers, J. Orchado, *Science* **273**, 1087 (1996); J. P. Severinghaus, T. Sowers, E. J. Brook, R. B. Alley, M. L. Bender, *Nature* **391**, 141 (1998); J. P. Severinghaus and E. J. Brook, *Science* **286**, 930 (1999).
25. We thank P. Marquet and L. Nuñez for field logistics; M. Arroyo, C. Villagrán, K. Zamora, A. Maldonado, Z. Naiman, C. Placzek, B. Saavedra, and H. Samaniego for field assistance; G. Cisneros, B. Gillis, and C. Holmgren for laboratory assistance; O. Matthei for grass identifications; J. Dohrenwend for map support; Geochronology Laboratory for conventional ^{14}C dates and the University of Arizona Accelerator Facility for accelerator mass spectrometry ^{14}C dates; J. Severinghaus for GISP2 methane data; L. Thompson for $\delta^{18}O$ and dust data from Sajama; and J. Cole, S. Jackson, M. Vuille, M. Cane, and A. Clement for discussions. This work was supported by an InterAmerican Institute grant to J.L.B. and V. Markgraf, National Geographic Society and NSF grants to J.Q. and J.L.B., and the U.S. Geological Survey. C.L. is supported by Comisión Nacional de Investigación Científica y Tecnología, Chile, with travel to Arizona provided by a U.S. Agency for International Development grant to B. Timmerman. J.A.R. is supported by a NASA grant.

12 May 2000; accepted 29 June 2000

Structural Evidence for Evolution of the β/α Barrel Scaffold by Gene Duplication and Fusion

Dietmar Lang,[1] Ralf Thoma,[2] Martina Henn-Sax,[3] Reinhard Sterner,[2,3,4] Matthias Wilmanns[1]*

The atomic structures of two proteins in the histidine biosynthesis pathway consist of β/α barrels with a twofold repeat pattern. It is likely that these proteins evolved by twofold gene duplication and gene fusion from a common half-barrel ancestor. These ancestral domains are not visible as independent domains in the extant proteins but can be inferred from a combination of sequence and structural analysis. The detection of subdomain structures may be useful in efforts to search genome sequences for functionally and structurally related proteins.

Enzymes from metabolic pathways are among the best-studied examples of protein function and structure. There are catabolic pathways, like glycolysis, or anabolic pathways, like tryptophan biosynthesis, where an almost complete database of protein structures is available. It is evident that many enzymes in these pathways have evolved either by gene duplication and fusion or by the assembly into functional oligomers (*1*, *2*). Molecular relations of proteins of the histidine and tryptophan biosynthesis pathways were postulated by structure prediction (*3*) and multisequence alignment methods (*4*). Many proteins in these pathways and other biological processes are folded as eightfold β/α barrels (*5*, *6*). Their evolution has been discussed (*7*, *8*) and has recently been mimicked in a directed evolution experiment (*9*). Here, we compare atomic structures of two enzymes in the histidine biosynthesis pathway and provide evidence for the evolution of β/α barrels from an ancestral half-barrel. The observation that ancestral folding units may comprise subdomain structural units has broad applications in searching genomic sequences for related gene products and their functional interactions in biological processes (*2*, *10*–*12*).

The crystal structures of the monomeric gene products HisA and HisF from the hyperthermophile *Thermotoga maritima* were deter-

[1]European Molecular Biology Laboratory (EMBL) Hamburg Outstation, EMBL c/o Deutsches Elektronen-Synchrotron (DESY), Notkestrasse 85, D-22603 Hamburg, Germany. [2]Abteilung für Biophysikalische Chemie, Biozentrum der Universität Basel, Klingelbergstrasse 70, CH-4056 Basel, Switzerland. [3]Abteilung für molekulare Genetik und Präparative Molekularbiologie, Institut für Mikrobiologie und Genetik, Georg-August-Universität Göttingen, Grisebachstrasse 8, D-37077 Göttingen, Germany. [4]Universität zu Köln, Institut für Biochemie, Otto-Fischer-Strasse 12-14, D-50674 Köln, Germany.

*To whom correspondence should be addressed. E-mail: wilmanns@embl-hamburg.de

mined at 1.85 and 1.45 Å resolution, respectively, using multiwavelength anomalous dispersion (MAD) phases of crystals with selenomethionine-substituted sequences (Table 1) (*13*). HisA and HisF share about 25% sequence identity (*14, 15*) and catalyze two successive reactions in histidine biosynthesis (*16*). HisA converts *N*′-[(5′-phosphoribosyl)-formimino]-5-aminoimidazol-4-carboxamid ribonucleotide (ProFAR) into the 5′-phosphoribulosyl isomer (PRFAR). HisF is part of a heterodimeric complex, which is a glutamine amidotransferase comprising the synthase subunit HisF and the glutaminase subunit HisH. HisF catalyzes the condensation of PRFAR and ammonia, which is provided by HisH, followed by the cleavage of the condensation product into 5-aminoimidazole-4-carboxamide ribotide (AICAR) and imidazoleglycerol phosphate (ImGP) (*16*). The HisF:HisH complex is a branch-point enzyme, because its two products ImGP and AICAR are further used in histidine biosynthesis and in the de novo purine biosynthesis, respectively.

The x-ray structures of HisA and HisF show that both enzymes are folded as β/α barrels (Fig. 1), as predicted (*3, 4*). Most β strands of each central β barrel are short (4 to 5 residues), except β1 and β5 (9 to 11 residues). The active sites in both enzymes are located at the COOH-terminal face of each β barrel, as indicated by the location of clusters of invariant residues in multiple sequence alignments (*15*) and the presence of two phosphate ions in the HisF structure, mimicking the two phosphate moieties of the HisF substrate (Fig. 1). The loops at the NH_2-terminal face of each β barrel are generally short and without any specific features. In contrast, several loops at the COOH-terminal face of the β barrel form extensive structures in both HisA and HisF.

In both enzymes, the loops at the COOH-terminal face display a twofold repeated struc-

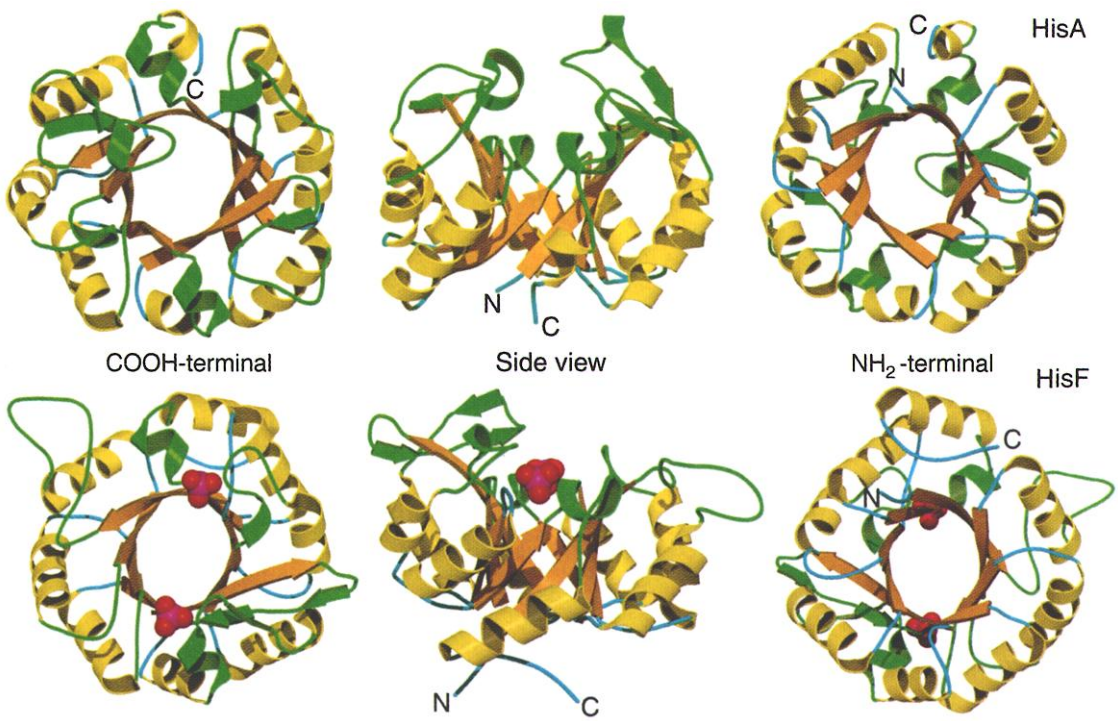

Fig. 1. Atomic structures of HisA (**upper panel**) and HisF (**lower panel**) from *Thermotoga maritima* in ribbon presentations (*29*). View from the COOH-terminal face of the central β barrel, left; side view, center; and view from the NH_2-terminal face of the barrel, right. HisF contains two phosphate ions bound to the active site, shown as space-filling models (red). The β strands and α helices of the central eightfold β/α barrel are in orange and yellow, respectively. Loops at the NH_2- and COOH-terminal faces of the barrel are in cyan and green, respectively. Some loops contain additional secondary structural elements. The NH_2- and COOH-termini are labeled when visible.

Table 1. X-ray data collection and phasing statistics.

Crystal	λ (Å)	d(min) (Å)	No. data	Comp.* (%)	Multiplicity	I/σ (last shell)	R_{sym}† (%)	X^2‡	Phasing power§	R_{cullis}‖
X-ray data collection										
HisA(SeMet)-peak	0.9787	2.34	17644	99.1/93.8	10.4	22.1 (8.0)	6.5 (15.1)	2.40	1.83	0.74
HisA(SeMet)-inflection	0.9791	2.34	17660	99.2/93.6	10.4	23.7 (6.9)	5.6 (14.8)	1.63	2.00	0.79
HisA(SeMet)-remote	0.9807	2.34	17595	98.8/92.6	9.7	24.1 (7.4)	5.1 (14.2)	0.95	0.79	0.97
HisA(SeMet)-"native"	0.9807	1.85	34941	97.4	5.8	17.0 (2.5)	4.8 (30.4)	–	–	–
HisF(SeMet)-peak	0.9796	1.85	17980	99.1/91.6	8.7	15.4 (9.2)	7.2 (13.0)	3.11	3.34	0.52
HisF(SeMet)-inflection	0.9789	1.85	17951	99.2/92.8	9.7	21.5 (11.4)	5.9 (11.3)	2.80	3.13	0.56
HisF(SeMet)-remote	0.9809	1.85	18037	98.6/91.0	7.5	33.3 (13.5)	4.0 (8.0)	0.88	0.99	0.96
HisF(wild-type)	0.909	1.42	37314	95.1	6.0	19.8 (10.3)	5.6 (11.3)	–	–	–

Crystal	Protein atoms	Solvent atoms	Ligand atoms	rmsd bond length (Å)	rmsd bond angles (°)	R_{cryst}¶ (%)	R_{free}¶ (%)	⟨B⟩ (Å²)
Structure refinement								
HisA	3798	547	0	0.005	1.28	18.8	24.6	20.8
HisF	1961	304	10	0.006	1.35	17.8	21.4	16.7

*Completeness of unique data/Friedel pairs. †$R_{sym} = \Sigma_{hkl}\Sigma_i|I_i(hkl) - \langle I(hkl)\rangle|\Sigma_{hkl}\Sigma_i I_i(hkl)$. ‡Weighted error estimate, as defined in the DENZO package (*13*). §Phasing power is defined as the ratio of the rms value of the heavy-atom structure factors amplitudes and the rms value of the lack-of-closure error. Statistics are on acentric data and their anomalous values. ‖R_{cullis} is the mean lack-of-closure error divided by the isomorphous/anomalous difference. Statistics are on acentric data and their anomalous values. ¶R_{cryst} and $R_{free} = \Sigma|F_{obs} - F_{calc}|/\Sigma F_{obs}$; R_{free} is calculated with 5% of the data that were not used for refinement.

tural pattern (Fig. 2), prompting a fourfold comparison of the NH_2-terminal halves (HisA-N, HisF-N) and the COOH-terminal halves (HisA-C, HisF-C) of each β/α barrel. The first loop in each half-barrel (pink loops 1 and 5) is approximately 20 residues long. It immediately turns and forms a small antiparallel β sheet with the COOH-terminus of the preceding long β strand 1 or 5 of the barrel (except in HisF-N). In each of the two enzymes, these loops 1 and 5 form the cleft of the active site. The next loop in each half-barrel (blue loops 2 and 6) contains a short one-turn helix (except in HisF-N). It is followed by a short loop (cyan loops 3 and 7) with a fixed length of five residues. The last loop in each half-barrel (green loops 4 and 8) contains another one-and-a-half turn helix. The presence of two phosphate ions in HisF, bound to loops 3 and 4, and 7 and 8, respectively, indicates a role of these loops in binding of the phosphate moieties of the respective substrates, as observed in other known β/α barrel enzymes (*17*).

Table 2. Structure and sequence similarities of half-barrels. The rms deviations for each pair of superimposed half-barrels are given in the upper right of the matrix. The percentage of identical residues of each structure-based pair-wise sequence alignment is given in the lower left of this matrix. The calculations were carried out with the program ALIGN—PDB (*28*), using all main-chain, nonhydrogen atoms for finding the optimum structural superposition.

	HisA-N	HisA-C	HisF-N	HisF-C
HisA-N	–	2.10 Å	1.41 Å	1.55 Å
HisA-C	23%	–	1.86 Å	1.75 Å
HisF-N	26%	22%	–	1.58 Å
HisF-C	15%	16%	16%	–

The half-barrel structures superimpose with rms deviations of 1.5 to 2.0 Å (Table 2). A structure-based sequence alignment of HisA-N, HisF-N, HisA-C, and HisF-C (Fig. 2B) reveals a number of residues that are not only invariant among the known sequences of each enzyme (*15*) but are located at structurally identical positions in all four half-barrels. There are two residues at the first loop of each barrel, an aspartate and a valine, that are invariant in all four half-barrel sequences. The position of each aspartate in the center of the active sites of HisA and HisF indicates a role in the catalytic functions of these enzymes (Fig. 2A). The role of the invariant valine is to position the NH_2-terminus of loops 1 and 5 onto the surface of the β/α barrel. In addition, there are three invariant glycine positions, one in a loop at the NH_2-terminal face connecting the first α helix (α1/α5) and the second β strand (β2/β6) of each half-barrel, and two in a GG motif in the third loop of the COOH-terminal face of each half-barrel. The overall fourfold alignment unambiguously identifies 22% (19 of 87) identical or similar residues (Fig. 2B), revealing a sequence and structural pattern that is common to the two barrel halves of the two enzymes.

These structural data strongly suggest evolution of HisA and HisF from a single common ancestral half-barrel, supporting previous proposals (*14, 15*). The complete conservation of an aspartate in the active sites in all four half-barrel sequences (Fig. 2B) suggests an evolutionary process through a broad functionality β/α barrel ancestor in which this residue could have played distinct roles in different catalytic mechanisms. This has prompted us to test HisA and HisF for their mutual residual activities (*18*). Indeed, HisF displays significant catalytic HisA activity, with a k_{cat}/K_M^{PRFAR} (specificity constant for PRFAR) of 0.1 mM^{-1} s^{-1} at 25°C. This activity is lost, however, in either of

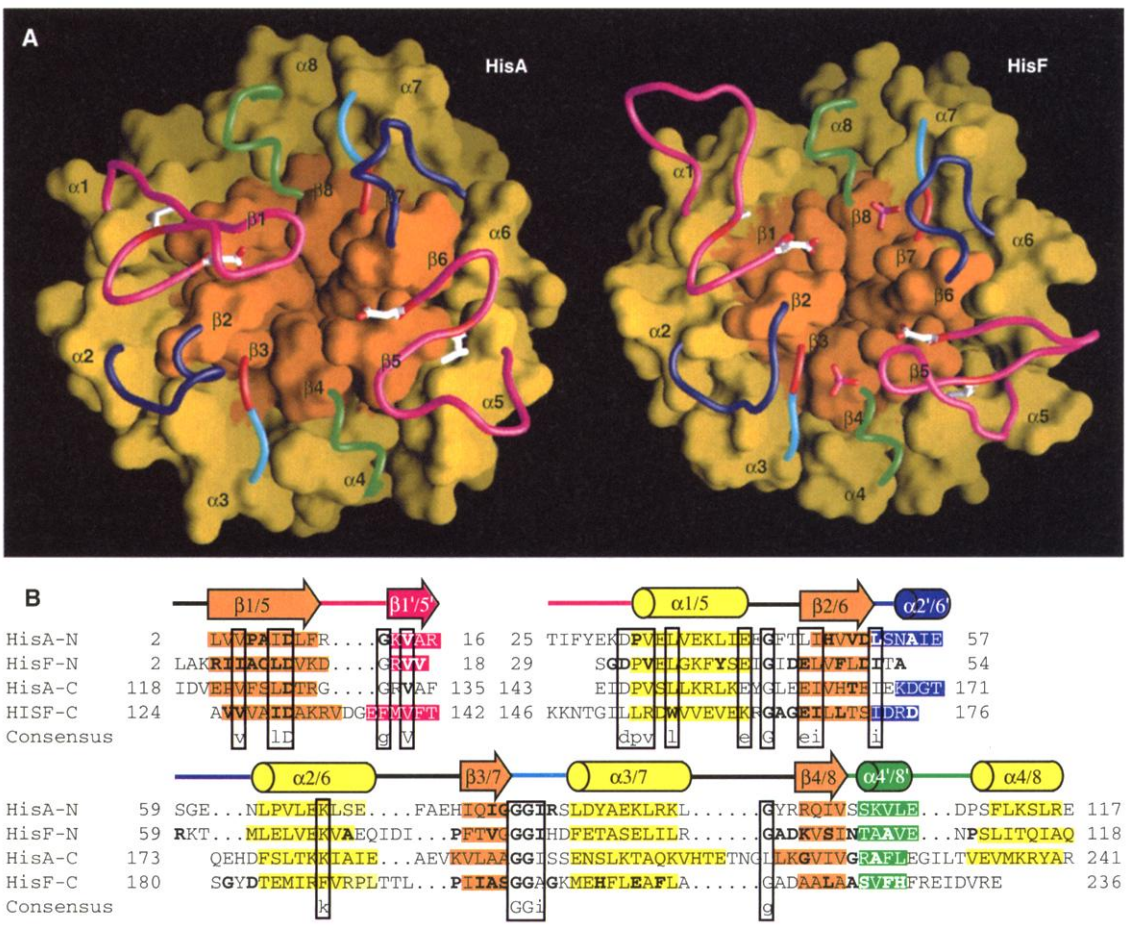

Fig. 2. Comparative analysis of HisA and HisF. (**A**) Surface presentation of HisA and HisF viewed from the COOH-terminal face of the β/α barrel containing the active site (*29*). The view is as in left panels of Fig. 1. The surface areas covering the β strands and the α helices of the β/α barrel are numbered and colored in orange and yellow, as in Fig. 1. The active site loops are excluded from the surface presentation and are displayed by colored tubes. Loops 1 and 5, pink; loops 2 and 6, blue; loops 3 and 7, cyan; and loops 4 and 8, green. Structural invariant residue positions in these loops [see panel (B)] are in red. The side chains of the invariant aspartate and valine residues in loops 1 and 5 and the two phosphate ions bound to the active site of HisF are shown as well. (**B**) Structure-based sequence alignment (*28*) of the NH_2- and COOH-terminal halves of HisA and HisF. The positions of the secondary structure elements are color coded as in (A). Residues that are conserved among sequences of one enzyme (*15*) are shown in bold. Residues that are similar in the structure alignment are boxed. Invariant and similar residues in the consensus are in capital and lowercase characters, respectively. The locations of the secondary structural elements are colored as in (A). The approximate consensus locations of the secondary structure elements and loops are also indicated above the alignment.

the two HisF mutants in which one of the two invariant aspartates has been replaced by an asparagine (D11N, D130N). Conversely, HisA does not show any detectable HisF activity under identical conditions, which is not surprising in light of the higher complexity of the HisF synthase reaction compared to the HisA isomerization reaction (*19*). Our data led to a model of the evolution of the HisA and HisF β/α barrels by two successive gene duplications (Fig. 3). In this model, the first gene duplication from an ancestral half-barrel sequence is followed by gene fusion and mutational adaptation of the initially identical half-barrel sequences into a complete β/α barrel with postulated broad functionality. The extant enzymes HisA and HisF result from a second gene duplication leading to recruitment and diversification of the present catalytic functions.

The similarity of HisA and HisF is reminiscent of a previously identified pair of related β/α barrel enzymes, TrpC and TrpF, which catalyze two successive reactions in tryptophan biosynthesis (*17*). The HisA and HisF, and TrpC and TrpF enzyme pairs support the Horowitz hypothesis of metabolic pathway evolution by subsequent gene duplication and diversification while retaining the binding mode for a common ligand (*20*). To detect more distant relationships of β/α barrels from different pathways, we searched the Protein Data Bank (1987 protein chains, currently) for structures similar to HisA and HisF (*21*). The three top-scoring entries, showing the highest similarity to HisA, are the three β/α barrel enzymes of the tryptophan biosynthesis pathway (TrpC, rank 1; TrpF, rank 2; and TrpA, rank 3). These three enzymes are also among the top 10 if HisF is used as structural template (ranks 4, 2, and 7, respectively), demonstrating distant but significant structural relations of β/α barrels between these two metabolic pathways. When the reaction mechanisms of these enzymes are compared, there is a strong interpathway similarity between TrpF and HisA, which both catalyze isomerization reactions by an Amadori rearrangement mechanism (*1, 16*). The TrpF and HisA pair fits well into another attractive hypothesis that considers binding to the transition state of chemically related reactions to direct evolution of enzymes (*22, 23*). The detection of these relations has opened opportunities to engineer enzymatic activities by in vitro evolution techniques using the β/α barrel scaffold. This potential has been recently demonstrated by the conversions of TrpC and HisA into TrpF (*9, 24*).

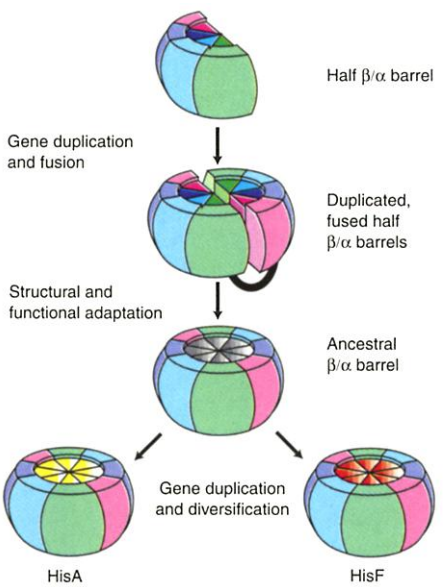

Fig. 3. Model for the evolution of the β/α barrel scaffold by twofold gene duplication. The first gene duplication generates two initially identical half-barrels that are then fused and adapted into an ancestral β/α barrel. A second gene duplication step leads to the diversification of the ancestral β/α barrel into two enzymes with distinct catalytic activities.

The currently available genomes provide a growing database of multidomain proteins that have evolved from gene fusion, either following duplication of initially identical genes or from genes with different function. The comparative analysis of their single-gene building blocks by computational methods allows the identification of a large number of functional relations in biological processes (*25*). HisA and HisF are the first β/α barrel enzymes with a detectable twofold repeat structure and can be regarded as prototype gene fusions leading to compact single-domain proteins, unlike many established examples of multidomain proteins (*26, 27*). Each half-barrel of these two enzymes contains a phosphate-binding motif that is imposed by the nature of their biphosphate substrates, ProFAR and PRFAR. The same motif is found in the COOH-terminal halves of a number of other β/α barrel enzymes, including those of the tryptophan biosynthesis (*17*), but not in their NH_2-terminal halves. This could indicate a half-barrel precursor for a large number of β/α barrels where, however, detectable relations might have been lost during the evolutionary diversification process. Therefore, the insights into the evolution of the histidine biosynthesis β/α barrel enzymes could allow reinvestigation of the evolutionary, structural, and functional relations of the β/α barrel family, which is likely the most widely used scaffold in soluble proteins. We anticipate that our approach to deconvolute extant proteins with a compact domain into small ancestral precursor domains is generally applicable to the genomic analysis of other protein fold families by computational and experimental methods.

References and Notes

1. C. Yanofsky, E. W. Miles, T. Bauerle, K. Kirschner, *The trp Operon and Tryptophan Biosynthesis in* Escherichia coli *and* Salmonella enterica, T. E. Creighton, Ed., vol. 4 of *The Encyclopedia of Molecular Biology* (Wiley, New York, 1999), pp. 2676–2689.
2. T. Dandekar, B. Snel, M. Huynen, P. Bork, *Trends Biochem. Sci.* **23**, 324 (1998).
3. M. Wilmanns and D. Eisenberg, *Proc. Natl. Acad. Sci. U.S.A.* **90**, 1379 (1993).
4. P. Bork, J. Gellerich, H. Groth, R. Hooft, F. Martin, *Protein Sci.* **4**, 268 (1995).
5. N. Nagano, E. G. Hutchinson, J. M. Thornton, *Protein Sci.* **8**, 2072 (1999).
6. G. A. Petsko, *Nature* **403**, 606 (2000).
7. D. Reardon and G. K. Farber, *FASEB J.* **9**, 497 (1995).
8. J. A. Gerlt, *Nature Struct. Biol.* **7**, 171 (2000).
9. M. M. Altamirano, J. M. Blackburn, C. Aguayo, A. R. Fersht, *Nature* **403**, 617 (2000).
10. E. M. Marcotte, M. Pellegrini, M. J. Thompson, T. O. Yeates, D. Eisenberg, *Nature* **402**, 83 (1999).
11. A. J. Enright, I. Iliopoulos, N. C. Kyrpides, C. A. Ouzounis, *Nature* **402**, 86 (1999).
12. A. R. Mendelsohn and R. Brent, *Science* **284**, 1948 (1999).
13. X-ray structure determination. Details of the expression, purification, and crystallization of HisA and HisF are described in [R. Thoma *et al.*, *FEBS Lett.* **454**, 1 (1999)]. Crystal form III of HisA was used for structure solution. MAD data of crystals containing selenomethionine–substituted HisA and HisF were collected at the energy tunable wiggler beamline BW7A at EMBL/DESY, Hamburg, at three different wavelengths each (Table 1). The native HisF data set was collected on beamline X11 at EMBL/DESY, Hamburg. All data were processed with the HKL suite [Z. Otwinowski and V. Minor, *Methods Enzymol.* **276**, 307 (1997)]. For the structure determination of HisF, initially five of six selenomethionines of one HisF molecule/asymmetric unit were located and refined. The HisA crystals contained two protein molecules per asymmetric unit with three selenomethionines each. Three of the six positions were initially found and refined. The phasing and subsequent structure solution was carried out using programs of the CCP4 suite [Collaborative Computational Project, *Acta Crystallogr. D* **50**, 760 (1994)], SHARP [E. LaFortelle, J. J. Irwin, G. Bricogne, in *Crystallographic Computing*, P. Bourne and K. Watenpaugh, Eds. (Oxford Science, Oxford, 1997), pp. 100–130], SOLVE [T. C. Terwilliger and J. Berendzen, *Acta Crystallogr. D* **55**, 849 (1999)], wARP [A. Perrakis, R. Morris, V. S. Lamzin, *Nature Struct. Biol.* **6**, 458 (1999)], REFMAC [G. N. Murshudov, A. A. Vagin, A. Lebedev, K. S. Wilson, E. J. Dodson, *Acta Crystallogr. D* **55**, 247 (1999)], CNS [A. T. Brünger *et al.*, *Acta Crystallogr. D* **54**, 905 (1998)], and the graphics program O [T. A. Jones, J.-Y. Zou, S. W. Cowan, M. Kjeldgaard, *Acta Crystallogr. A* **47**, 110 (1991)]. The final refinement of the two structures was carried out using high-resolution data sets to 1.45 and 1.85 Å resolution, respectively. Further statistics of the refined models are given in Table 1.
14. R. Fani, P. Lio, I. Chiarelli, M. Bazzicalupo, *J. Mol. Evol.* **38**, 489 (1994).
15. R. Thoma, M. Schwander, W. Liebl, K. Kirschner, R. Sterner, *Extremophiles* **2**, 379 (1998).
16. P. Alifano *et al.*, *Microbiol. Rev.* **60**, 44 (1996).
17. M. Wilmanns, C. C. Hyde, D. R. Davies, K. Kirschner, J. N. Jansonius, *Biochemistry* **30**, 9161 (1991).
18. Residual catalytic activities: For measuring residual HisA activity of HisF, 20 μM ProFAR (substrate of HisA) was dissolved in 50 mM Tris-HCl buffer (pH 8.0 at 25°C), containing 1 mM EDTA and 1 mM dithiothreitol. We added 350 mM ammonium acetate as source for ammonia, which is provided by the glutaminase activity of HisH under in vivo conditions. Addition of 20 μM HisF resulted in a significant decrease of the absorption at 300 nm wavelength, reaching its final value after about 2 hours. Therefore, HisF first converted ProFAR into its natural substrate PRFAR (residual HisA reaction), and then catalyzed its condensation with ammonia to yield the products AICAR and ImGP (*19*). The progress curve was normalized using $\Delta\varepsilon_{300}$(ProFAR-AICAR) = 5.637 $mM^{-1}\,cm^{-1}$ and analyzed with the integrated Michaelis-Menten equation [U. Hommel, M. Eberhard, K. Kirschner, *Biochemistry* **34**, 5429 (1995)]. Analogous experiments were performed in the presence of 15 μM of the HisF point mutants D11N or D130N. For these mutants, no significant decrease of the absorption at 300 nm could be detected within 2 hours, even in the presence of low concentrations (1 μM) of wild-type HisF as helper enzyme. To measure residual HisF activity of HisA, the assay was carried out as described above, however, with addition of 20 μM HisA instead of

HisF. No significant decrease of the absorption at 300 nm was detected within 2 hours.
19. T. J. Klem and V. J. Davisson, *Biochemistry* **32**, 5177 (1993).
20. N. H. Horowitz, *Proc. Natl. Acad. Sci. U.S.A.* **31**, 153 (1945).
21. L. Holm and C. Sander, *Nucleic Acids Res.* **26**, 316 (1998).
22. J. A. Gerlt and P. C. Babbitt, *Curr. Opin. Chem. Biol.* **2**, 607 (1998).
23. M. S. Hasson *et al.*, *Proc. Natl. Acad. Sci. U.S.A.* **95**, 10396 (1998).
24. C. Jürgens *et al.*, *Proc. Natl. Acad. Sci. U.S.A.* **97**, 9925 (2000).
25. E. M. Marcotte *et al.*, *Science* **285**, 751 (1999).
26. R. F. Doolittle, *Annu. Rev. Biochem.* **64**, 287 (1995).
27. B. Morgenstern and W. R. Atchley, *Mol. Biol. Evol.* **16**, 1654 (1999).
28. G. E. Cohen, *J. Appl. Crystallogr.* **30**, 1160 (1997).
29. The figures were prepared using the graphics software MOLSCRIPT version 2.1 [P. J. Kraulis, *J. Appl. Crystallogr.* **24**, 946 (1991)] and GRASP version 1.3 [A. Nicholls, K. A. Sharp, N. Honig, *Proteins* **11**, 281 (1991)].

30. We thank K. Kirschner for discussions, V. Lamzin for comments on the manuscript, and S. Beismann-Driemeyer for the provision of HisF mutants. M.H.-S. is a fellow of the Hans-Böckler-Stiftung. The atomic coordinates have been deposited in the Protein Data Bank (code for HisA: 1QO2; code for HisF: 1THF). This work was supported by the Deutsche Forschungsgemeinschaft (grants STE 891/2-1, STE 891/2-2, and STE 891/3-1 to R.S., WI 1058/5-1 and WI 1058/5-2 to M.W., and a Heisenberg Fellowship to R.S.).

20 April 2000; accepted 6 July 2000

Selective Inhibition of NF-κB Activation by a Peptide That Blocks the Interaction of NEMO with the IκB Kinase Complex

Michael J. May,[1] Fulvio D'Acquisto,[1] Lisa A. Madge,[2] Judith Glöckner,[1] Jordan S. Pober,[2] Sankar Ghosh[1]*

Activation of the transcription factor nuclear factor (NF)–κB by proinflammatory stimuli leads to increased expression of genes involved in inflammation. Activation of NF-κB requires the activity of an inhibitor of κB (IκB)-kinase (IKK) complex containing two kinases (IKKα and IKKβ) and the regulatory protein NEMO (NF-κB essential modifier). An amino-terminal α-helical region of NEMO associated with a carboxyl-terminal segment of IKKα and IKKβ that we term the NEMO-binding domain (NBD). A cell-permeable NBD peptide blocked association of NEMO with the IKK complex and inhibited cytokine-induced NF-κB activation and NF-κB–dependent gene expression. The peptide also ameliorated inflammatory responses in two experimental mouse models of acute inflammation. The NBD provides a target for the development of drugs that would block proinflammatory activation of the IKK complex without inhibiting basal NF-κB activity.

The regulatory protein NEMO (also named IKKγ) is required for proinflammatory activation of the IκB-kinase (IKK) complex (*1*–*5*). We surmised that prevention of the NEMO-IKK interaction would inhibit signal-induced NF-κB activation and, therefore, attempted to identify the mechanism of interaction between NEMO and IKKβ. We analyzed the interaction of NEMO fused at its NH_2-terminus to glutathione *S*-transferase (GST-NEMO, see Fig. 1A) with IKKβ mutants lacking the catalytic, leucine zipper, and helix-loop-helix (HLH) domains [Fig. 1A and (*6*)]. None of the mutants interacted with GST, whereas all three COOH-terminal fragments (307–756, 458–756, and 486–756) interacted with GST-NEMO [Fig. 1A and (*7*)]. None of the NH_2-terminal fragments (1–458, 1–605, or 1–644) precipitated with GST-NEMO, demonstrating that NEMO interacts with the COOH-terminus of IKKβ distal to the HLH. An IKKβ mutant consisting of only residues 644 to 756 associated with GST-NEMO, confirming that this region mediates interaction between the molecules (Fig. 1B). Furthermore, IKKβ(644–756) dose-dependently inhibited cytokine-induced NF-κB activation in transfected HeLa cells [Fig. 1C and (*6*, *8*)]. The most likely explanation for this result is that overexpressed IKKβ(644–756) associates with endogenous NEMO and prevents recruitment of regulatory proteins to the IKK-complex.

To identify the domain of NEMO (*1*–*3*, *9*) required for association with IKKβ, we analyzed the interaction of GST-IKKβ(644–756) with truncation mutants of NEMO (Fig. 1D). IKKβ(644–756) associated with NEMO fragments 1–196, 1–302, and 44–419 but not 197–419 or 86–419, indicating that the interaction domain lies between residues 44 and 86. A deletion mutant lacking this α-helical region (residues 50–93, del.αH) did not interact with IKKβ(644–756) (Fig. 1E) and inhibited tumor necrosis factor–α (TNF-α)–induced NF-κB activity (Fig. 1F), confirming the dominant-negative effects of the NEMO COOH-terminus (*2*, *3*). These findings suggest that the NH_2-terminus of NEMO anchors it to the IKK-complex, leaving the remainder of the molecule accessible for interacting with regulatory proteins.

The IKKβ COOH-terminus contains a region with identity to IKKα (denoted α_1), a serine-rich domain (*10*), and a serine-free region (Fig. 2A). Analysis of IKKβ mutants omitting each of these segments indicated that NEMO associates with the COOH-terminus after residue 734 (Fig. 2A). The region of IKKβ from F734 to T744 [α_2 in Fig. 2B (*11*)] contains a segment that is identical to the equivalent sequence in IKKα. The IKKβ sequence then extends for 12 residues forming a glutamate-rich region (Fig. 2B) that we speculated would be the NEMO interaction domain. However, a truncation mutant omitting this region (1–744) associated with GST-NEMO (Fig. 2C). Thus, the NEMO-interaction domain of IKKβ appears to be within the α_2-region of the COOH-terminus.

We next used the IKKβ(1–744) and (1–733) mutants to determine the effects of NEMO association on IKKβ activity and found that IKKβ(1–733) induced NF-κB activation that was approximately 1.5 to 2 times that induced by wild-type IKKβ (Fig. 2D). Furthermore, NF-κB activity induced by IKKβ(1–744) was identical to that induced by wild-type IKKβ. Thus, NEMO may maintain basal IKKβ activity as well as regulate its signal-induced activation.

Because the α_2-region of IKKβ resembles the COOH-terminus of IKKα (Fig. 2B), we tested the ability of IKKα to interact with NEMO (*7*). IKKα and IKKβ expressed in wheat germ extract both associated with GST-NEMO demonstrating that the individual interactions are direct (Fig. 3A). Further analysis revealed that IKKα interacts with NEMO through the COOH-terminal region containing the six amino

[1]Section of Immunobiology and Department of Molecular Biophysics and Biochemistry, Howard Hughes Medical Institute, Yale University School of Medicine, New Haven, CT 06510, USA. [2]Interdepartmental Program in Vascular Biology and Transplantation, Boyer Center for Molecular Medicine, Yale University School of Medicine, New Haven, CT 06536, USA.

*To whom correspondence should be addressed. E-mail: sankar.ghosh@yale.edu